

Bipolar thermoelectric effects in semiconducting carbon nanotubes: Description in terms of one-dimensional Dirac electrons

Takahiro Yamamoto¹ and Hidetoshi Fukuyama²

¹ Department of Liberal Arts, Faculty of Engineering, Tokyo University of Science, Katsushika, Tokyo 125-8585, Japan

² Department of Applied Physics, Faculty of Science, Tokyo University of Science, Shinjuku, Tokyo 162-8601, Japan

The thermoelectric effects in semiconducting single-walled carbon nanotubes (SWCNTs) are investigated based on the linear response theory combined with the thermal Green's function method. It is shown that the electronic states near the lowest conduction band minimum and the highest valence band maximum can be effectively described in terms of one-dimensional (1D) Dirac electrons to which a theoretical scheme is developed to describe the thermoelectric responses making it possible to study the effects of inter-band impurity scattering and in-gap states. Using the proposed scheme, the bipolar thermoelectric effects (*i.e.*, the sign inversion of the Seebeck coefficient) in semiconducting SWCNTs observed in recent experiments are explained. Moreover, the temperature dependence of the Seebeck coefficient of semiconducting SWCNTs at low temperature is clarified.

KEYWORDS: Seebeck coefficient, power factor, Dirac electron, carbon nanotube, linear response theory, thermal Green's function

1. Introduction

The development of high-performance thermoelectric materials is important for sustainable energy production. Hicks and Dresselhaus¹⁾ proposed that significant enhancements in the thermoelectric performance of materials could be realized by employing one-dimensional (1D) semiconductors. Various 1D materials exhibiting high thermoelectric performance have since been discovered.²⁻⁶⁾ Single-walled carbon nanotubes (SWCNTs), which are rolled up graphene in cylindrical form, have received particular interest as high-performance and flexible thermoelectric 1D materials.⁷⁻²⁴⁾ At present, the reported maximum power factor of SWCNTs is $\sim 700 \mu\text{Wm}^{-1}\text{K}^{-2}$ at 298 K,²¹⁾ which is comparable to that of high-performance inorganic thermoelectric materials.

Recently, the present authors theoretically demonstrated that “band-edge engineering” is crucial for the development of high-performance thermoelectric materials using impurity-doped semiconducting SWCNTs as an example.²⁴⁾ For band-edge engineering, the chemical potential μ of SWCNTs has been experimentally adjusted via chemical adsorption on the SWCNT surface,^{8,15,19)} encapsulation of molecules inside an SWCNT,¹⁸⁾ and carrier injection into an SWCNT by applying a gate voltage using a field-effect transistor (FET) setup.^{12,13)} In view of the FET experiment,^{12,13)} which clarified the bipolar thermoelectric effect of SWCNTs (*i.e.*, the sign inversion of the Seebeck coefficient from positive (p-type) to negative (n-type) when the gate voltage is changed), the present study investigates this bipolar effect theoretically based on the conduction and valence bands, described as 1D Dirac electrons in order to treat the effects of disorder induced coupling between the bands in a unified way²⁵⁾ (see Appendix A).

2. Theory of Thermoelectric Effects of Dirac Electrons in One-Dimensional Solids

2.1 Dirac electrons in one-dimensional solids with disorder

This section gives a brief review of 1D Dirac electrons in solids with disorder. The Hamiltonian of 1D Dirac electrons

in an impurity disorder potential is given by

$$\mathcal{H} = \int_{-\infty}^{\infty} dx \Psi^\dagger(x, t) H(x) \Psi(x, t) \quad (1)$$

with the local Hamiltonian matrix

$$H(x) = -i\hbar v \sigma_x \frac{\partial}{\partial x} + \Delta \sigma_z + U(x), \quad (2)$$

where \hbar is the Dirac constant, Δ is one half of the band gap, v is the velocity of a Dirac electron in the high-energy region of $|E| \gg \Delta$, σ_x and σ_z are the x and z components of Pauli matrices,

$$\sigma_x = \begin{pmatrix} 0 & 1 \\ 1 & 0 \end{pmatrix} \quad \text{and} \quad \sigma_z = \begin{pmatrix} 1 & 0 \\ 0 & -1 \end{pmatrix}, \quad (3)$$

respectively, and $U(x)$ is an impurity potential.

In Eq. (1), the field operators $\Psi(x, t)$ and $\Psi^\dagger(x, t)$ are defined as the following column and row vectors,

$$\Psi(x, t) \equiv \begin{pmatrix} \psi_1(x, t) \\ \psi_2(x, t) \end{pmatrix} \quad \text{and} \quad \Psi^\dagger(x, t) \equiv (\psi_1^\dagger(x, t), \psi_2^\dagger(x, t)), \quad (4)$$

respectively. Here, $\psi_n^\dagger(x, t)$ and $\psi_n(x, t)$ are the fermionic creation and annihilation field operators in the Heisenberg picture and satisfy the Heisenberg equations $i\hbar \frac{d\psi_n(x, t)}{dt} = [\psi_n(x, t), \mathcal{H}]$ and $i\hbar \frac{d\psi_n^\dagger(x, t)}{dt} = [\psi_n^\dagger(x, t), \mathcal{H}]$, respectively. Thus, it can be easily proven that $\Psi(x, t)$ and $\Psi^\dagger(x, t)$ satisfy the Schrödinger equation

$$i\hbar \frac{d\Psi(x, t)}{dt} = H(x) \Psi(x, t) \quad (5)$$

and its Hermitian conjugate

$$-i\hbar \frac{d\Psi^\dagger(x, t)}{dt} = (H(x) \Psi(x, t))^\dagger. \quad (6)$$

Performing the Fourier transform of $\Psi^\dagger(x, t)$ as

$$\Psi^\dagger(x, t) = \frac{1}{\sqrt{L}} \sum_k e^{-ikx} \Phi_k^\dagger(t) \quad (7)$$

with $\Phi_k^\dagger(t) \equiv (c_{1k}^\dagger(t), c_{2k}^\dagger(t))$ and using

$$U(x) = \sum_q e^{iqx} U(q), \quad (8)$$

the 1D Dirac Hamiltonian in Eq. (1) can be rewritten as

$$\mathcal{H} = \sum_k \Phi_k^\dagger H_0(k) \Phi_k + \sum_{k,q} \Phi_{k+q}^\dagger U(q) \Phi_k, \quad (9)$$

where $H_0(k)$ is the Hamiltonian density of a 1D free Dirac electron in k space, which is given by

$$H_0(k) = \hbar v k \sigma_x + \Delta \sigma_z \quad (10)$$

$$= \begin{pmatrix} \Delta & \hbar v k \\ \hbar v k & -\Delta \end{pmatrix}. \quad (11)$$

The eigenvalues of $H_0(k)$ in Eq. (11) can be easily obtained as

$$E_\pm(k) = \pm \sqrt{\Delta^2 + (\hbar v k)^2}, \quad (12)$$

where \pm corresponds the conduction (+) and valence (-) bands, respectively. Thus, the band gap is given by $E_g \equiv E_+(0) - E_-(0) = 2\Delta$.

2.2 General theory of thermoelectric responses

The thermoelectric effect is typically characterized by the Seebeck coefficient, S , which is defined as the voltage induced by a finite temperature gradient along a given direction (herein the x -direction) under the condition that there is no electrical current (*i.e.*, $J = 0$) along that direction. This can be written as

$$S \equiv - \left(\frac{\Delta V}{\Delta T} \right)_{J=0}, \quad (13)$$

where ΔV is the induced voltage and ΔT is the temperature difference between the two ends of the material.

In the presence of both an electric field \mathcal{E} and a temperature gradient dT/dx along the x -direction, the current density J is generally given by

$$J = L_{11} \mathcal{E} - \frac{L_{12}}{T} \frac{dT}{dx} \quad (14)$$

within the linear response regime with respect to \mathcal{E} and dT/dx . Here, L_{11} and L_{12} are the electrical conductivity and the thermoelectrical conductivity, respectively. The zero-current condition ($J = 0$) leads to $L_{11} \mathcal{E} = \frac{L_{12}}{T} \frac{dT}{dx}$. Because the electric field and the temperature gradient can be written as $\mathcal{E} = -\Delta V/L$ and $dT/dx = \Delta T/L$, respectively, for a spatially uniform system with length L (assumed here), S as defined in Eq. (13) can be expressed in terms of the response functions L_{11} and L_{12} as

$$S = \frac{1}{T} \frac{L_{12}}{L_{11}}. \quad (15)$$

One of the figures of merit for thermoelectric materials is the power factor, PF , defined as

$$PF \equiv \sigma S^2 = \frac{1}{T^2} \frac{L_{12}^2}{L_{11}}. \quad (16)$$

It should be noted that the basic quantities used for the thermoelectric responses of materials are L_{11} and L_{12} rather than S and PF .

2.3 Microscopic representation of L_{11} and L_{12}

L_{11} and L_{12} are expressed in terms of the J_e - J_e correlation function and the J_e - J_Q correlation function, respectively, where J_e and J_Q are the electronic current and the thermal current, respectively.^{26,27)} Microscopic justification for calculating L_{11} based on the J_e - J_e correlation function and L_{12} based on the J_e - J_Q correlation function was first given by Kubo in 1957²⁸⁾ and Luttinger in 1964,²⁹⁾ respectively. This subsection presents the explicit expressions of L_{11} and L_{12} for 1D Dirac electrons with an impurity potential based on the thermal Green's function formalism.

According to the linear response theory, the thermoelectrical conductivity L_{12} can be obtained as

$$L_{12} = - \lim_{\omega \rightarrow 0} \frac{\chi_{12}^R(\omega) - \chi_{12}^R(0)}{i\omega}, \quad (17)$$

$$\chi_{12}^R(\omega) = \chi_{12}(i\omega_\lambda) \Big|_{i\omega_\lambda \rightarrow \hbar\omega + i\delta}, \quad (18)$$

where $\chi_{12}(i\omega_\lambda)$ is the correlation function between the electrical current J_e and the thermal current J_Q , expressed as

$$\chi_{12}(i\omega_\lambda) = \frac{1}{V} \int_0^\beta d\tau \langle T_\tau \{ J_e(\tau) J_Q(0) \} \rangle e^{i\omega_\lambda \tau}, \quad (19)$$

where $\beta \equiv 1/(k_B T)$ is the inverse temperature, T_τ is the imaginary-time-ordering operator, $\langle \dots \rangle$ denotes the thermal average, and V is the volume of a system.

Now, $J_e(\tau)$ and $J_Q(\tau)$ for 1D Dirac electrons with a disorder potential are needed. The electric current carried by 1D Dirac electrons is given by

$$J_e(t) = -e \sum_k \Phi_k^\dagger(t) v(k) \Phi_k(t), \quad (20)$$

where $e(> 0)$ is the elementary charge and $v(k)$ is a 2×2 velocity matrix, which is given by

$$v(k) = \frac{1}{\hbar} \frac{\partial H_0(k)}{\partial k} = v \sigma_x = \begin{pmatrix} 0 & v \\ v & 0 \end{pmatrix}. \quad (21)$$

The thermal current $J_Q(t)$ is expressed as $J_Q(t) = J_E(t) + \frac{\hbar}{e} J_e(t)$, where the energy current $J_E(t)$ is defined as

$$J_E(t) = \frac{d\mathcal{A}(t)}{dt} \quad (22)$$

with energy polarization

$$\mathcal{A}(t) = \frac{1}{2} \int_{-\infty}^{\infty} dx \Psi^\dagger(x, t) \left(\frac{\sin Qx}{Q} H(x) + H(x) \frac{\sin Qx}{Q} \right) \Psi(x, t). \quad (23)$$

Here, Q is a parameter used to control the effects of the unbounded variable x and should be set to zero in the final step of a calculation.³⁰⁾ Using Eqs. (5) and (6), Eq. (22) is calculated as

$$J_E(t) = \frac{v}{2} \int_{-\infty}^{\infty} dx \Psi^\dagger(x, t) \{ \sigma_x H(x) + H(x) \sigma_x \} \Psi(x, t). \quad (24)$$

The derivation of Eq. (24) is given in Appendix B. Substituting Eqs. (7) and (8) into Eq. (24) yields

$$J_E(t) = \frac{1}{2} \sum_k \left[\Phi_k^\dagger(t) \{ v(k) H_0(k) + H_0(k) v(k) \} \Phi_k(t) + \sum_q \Phi_{k+q}^\dagger(t) \{ v(k+q) U(q) + U(q) v(k) \} \Phi_k(t) \right], \quad (25)$$

where $H_0(k)$ is the Hamiltonian density of 1D free Dirac elec-

trons in Eq. (11).

In the imaginary-time Heisenberg picture ($t \rightarrow -i\tau$), the electric current is expressed as

$$J_e(\tau) = -e \int_{-\infty}^{\infty} dx \bar{\Phi}_k(\tau) v(k) \Phi_k(\tau), \quad (26)$$

where $\bar{\Phi}_k(\tau) \equiv (\bar{c}_{1k}(\tau), \bar{c}_{2k}(\tau)) = (e^{\tau H} c_{1k}^\dagger e^{-\tau H}, e^{\tau H} c_{2k}^\dagger e^{-\tau H})$. Similarly, the energy current is given by

$$J_E(\tau) = -\frac{1}{2e} \sum_k \left[\left\{ \bar{\Phi}_k(\tau) H_0(k) + \sum_q \bar{\Phi}_{k+q}(\tau) U(q) \right\} J_e \Phi_k(\tau) + \bar{\Phi}_k(\tau) J_e \left\{ H_0(k) \Phi_k(\tau) + \sum_q U(q) \Phi_{k-q}(\tau) \right\} \right], \quad (27)$$

where the current matrix $J_e = -ev\sigma_x$. As first noted by Johnson and Mahan,³¹⁾ Eq. (27) can be rewritten as

$$J_E(\tau) = -\frac{1}{2e} \sum_k \left[\frac{d\bar{\Phi}_k(\tau)}{d\tau} J_e \Phi_k(\tau) - \bar{\Phi}_k(\tau) J_e \frac{d\Phi_k(\tau)}{d\tau} \right] \quad (28)$$

by using the relations

$$\frac{d\Phi_k(\tau)}{d\tau} = -H_0(k) \Phi_k(\tau) - \sum_q U(q) \Phi_{k-q}(\tau), \quad (29)$$

$$\frac{d\bar{\Phi}_k(\tau)}{d\tau} = \bar{\Phi}_k(\tau) H_0(k) + \sum_q \bar{\Phi}_{k+q}(\tau) U(q), \quad (30)$$

which are derived from $dc_{nk}(\tau)/d\tau = [H, c_{nk}(\tau)]$ and $d\bar{c}_{nk}(\tau)/d\tau = [H, \bar{c}_{nk}(\tau)]$. Using Eq. (28), the correlation function $\chi_{12}(i\omega_\lambda)$ is expressed in terms of the impurity-averaged thermal Green's function $\mathcal{G}(k, i\epsilon_n) \equiv \langle \mathcal{G}(k, k', i\epsilon_n) \rangle_{\text{imp}}$ as

$$\chi_{12}(i\omega_\lambda) = -\frac{ev^2}{V\beta} \sum_n \left(\frac{i\epsilon_n + i\epsilon_{n+}}{2} - \mu \right) \times \sum_k \text{Tr} [\sigma_x \mathcal{G}(k, i\epsilon_n) \tilde{\sigma}_x(k) \mathcal{G}(k, i\epsilon_{n+})] \quad (31)$$

with $\epsilon_{n+} \equiv \epsilon_n + \omega_\lambda$ and $\tilde{\sigma}_x(k)$ is given as $\tilde{\sigma}_x(k) = \sigma_x + \sigma'_x(k)$ with

$$\sigma'_x(k) = \sum_{k', k'', k'''} \langle U(k-k') \mathcal{G}(k', k'', i\epsilon_n) \tilde{\sigma}_x(k'') \times \mathcal{G}(k'', k''', i\epsilon_n) U(k'''-k) \rangle_{\text{imp}} \quad (32)$$

that gives the vertex correction for the current operator. In the following discussion, we assume that the vertex correction is neglected, *i.e.*, $\tilde{\sigma}_x \rightarrow \sigma_x$. In Eq. (31), $\mathcal{G}(k, i\epsilon_n)$ is given by a 2×2 matrix as

$$\mathcal{G}(k, i\epsilon_n) = \begin{pmatrix} \mathcal{G}_{11}(k, i\epsilon_n) & \mathcal{G}_{12}(k, i\epsilon_n) \\ \mathcal{G}_{21}(k, i\epsilon_n) & \mathcal{G}_{22}(k, i\epsilon_n) \end{pmatrix}, \quad (33)$$

where $\mathcal{G}(k, i\epsilon_n)$ is defined by the Fourier transform of $\mathcal{G}_{nm}(k, \tau) \equiv -\langle T_\tau \{ c_{nk}(\tau) \bar{c}_{mk}(0) \} \rangle$,

$$\mathcal{G}_{nm}(k, i\epsilon_n) = \int_0^\beta d\tau \mathcal{G}_{nm}(k, \tau) e^{i\epsilon_n \tau}. \quad (34)$$

The summation over n in Eq. (31) can be transformed into a contour integral in the complex energy space. Taking the limit of $\omega \rightarrow 0$ after the analytic continuation $i\omega_\lambda \rightarrow \hbar\omega + i\delta$ yields

the expression of L_{12} as

$$L_{12} = -\frac{1}{e} \int_{-\infty}^{\infty} dE \left(-\frac{\partial f(E - \mu)}{\partial E} \right) (E - \mu) \alpha(E), \quad (35)$$

where $f(E) = [1 + \exp\{(E - \mu)/k_B T\}]^{-1}$ is the Fermi-Dirac distribution function and $\alpha(E)$ is often called the spectral conductivity, which is expressed as

$$\alpha(E) = \frac{\hbar e^2 v^2}{2\pi V} \sum_k \text{Tr} \left[\sigma_x G^A(k, E) \sigma_x G^R(k, E) - \text{Re} \left\{ \sigma_x G^R(k, E) \sigma_x G^R(k, E) \right\} \right] \quad (36)$$

by use of the retarded/advanced Green's function,

$$G^{R/A}(E, k) = \left\{ EI - H_0(k) - \Sigma^{R/A}(E, k) \right\}^{-1}, \quad (37)$$

where I is the 2×2 identity matrix. The expression of L_{12} in Eq. (35) was first proposed for general cases by Sommerfeld and Bethe³²⁾ in 1933, and subsequently by Mott and Jones³³⁾ and by Wilson³⁴⁾ based on Boltzmann transport theory. Recently, Ogata and Fukuyama clarified the range of validity of the Sommerfeld and Bethe relation expressed as Eq. (35) for single-band systems with a disorder potential, electron-phonon coupling, and electron correlations as well as for multi-band disorder systems based on the Luttinger-Kohn representation.³⁰⁾

Using the expression of $\alpha(E)$ in Eq. (36), the electrical conductivity L_{11} of 1D Dirac electrons in a disorder potential is given by

$$L_{11} = \int_{-\infty}^{\infty} dE \left(-\frac{\partial f(E - \mu)}{\partial E} \right) \alpha(E). \quad (38)$$

3. Electronic States and Thermoelectric Responses of 1D Dirac Electrons

In this section, the thermoelectric effects of 1D Dirac electrons in a disorder potential are studied based on the thermal Green's function formalism using the self-energy corrections of Green's functions. The following subsections present two methods for treating self-energy correction: the constant- τ approximation and the self-consistent Born approximation.

3.1 Constant- τ approximation

As the simplest treatment of self-energy correction for a disorder potential, the constant- τ approximation (*i.e.*, $\Sigma^{R/A} = \mp i(\hbar/2\tau)I$) is employed here and vertex correction is neglected. Here, τ is the relaxation time of a Dirac electron scattered by a disorder potential, which is assumed to be independent of the energy E and the wavenumber k . Although this constant- τ approximation is simple, the approximation is very useful for obtaining an overview of the thermoelectric response of 1D Dirac electrons in a disorder potential.

3.1.1 Density of states and spectral conductivity

In the constant- τ approximation, the retarded and advanced Green's functions for a 1D Dirac electron are given by

$$G^{R/A}(E, k) = \left\{ \left(E \pm i \frac{\hbar}{2\tau} \right) I - (\hbar v k \sigma_x + \Delta \sigma_z) \right\}^{-1}, \quad (39)$$

which leads to the following expressions for the density of states (DOS) $\rho(E)$ per unit cell of the system and spectral con-

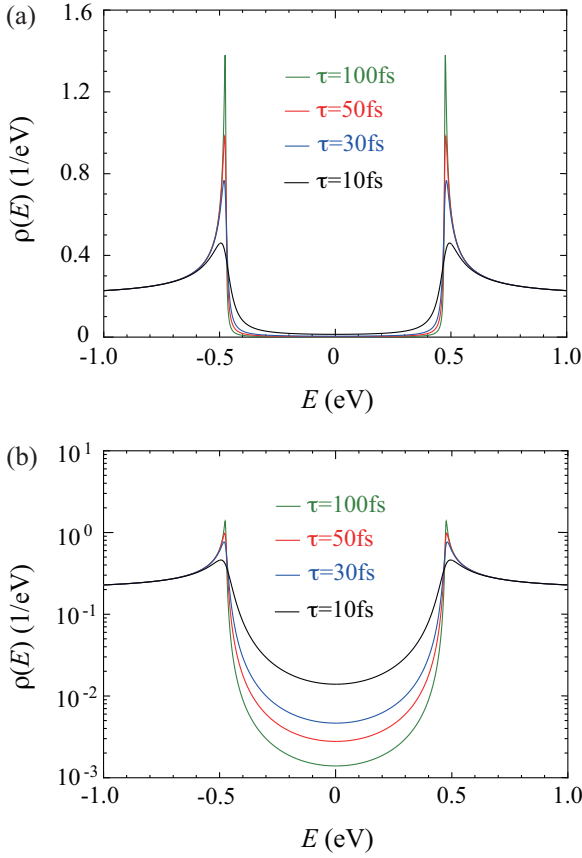


Fig. 1. (Color online) (a) Density of states near the band gap of (10,0) SWCNTs per spin and orbital for $\tau = 10$ (black curve), 30 (blue curve), 50 (red curve), and 100 fs (green curve) calculated using the constant- τ approximation and (b) the corresponding semi-log plots.

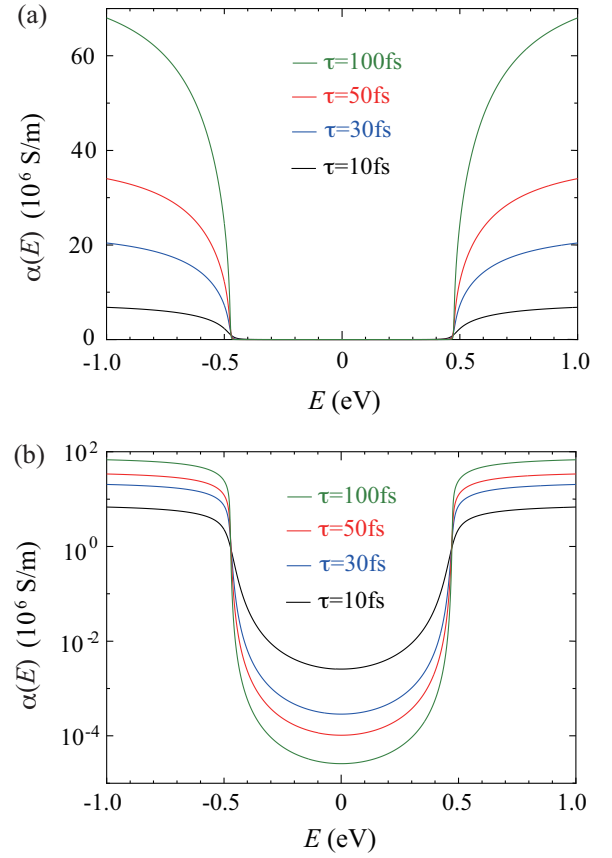


Fig. 2. (Color online) (a) Spectral conductivities of (10,0) SWCNTs for $\tau = 10$ (black curve), 30 (blue curve), 50 (red curve), and 100 fs (green curve) calculated using the constant- τ approximation and (b) the corresponding semi-log plots.

ductivity $\alpha(E)$

$$\rho(E) = -\frac{1}{\pi N} \text{Tr} \sum_k \text{Im} G^R(k, E) \quad (40)$$

$$= \frac{a}{\pi(\hbar v)^2} \text{Im} \left(\frac{\gamma + iE}{k_+} \right) \quad (41)$$

and

$$\alpha(E) = i \frac{e^2}{\hbar} \frac{1}{\pi A} \frac{1}{k_+ - k_-} \left\{ 1 - \frac{1}{k_+ k_-} \frac{E^2 + \gamma^2 - \Delta^2}{(\hbar v)^2} \right\}, \quad (42)$$

with $\gamma \equiv \hbar/2\tau$. Here, N is the total number of unit cells, a is the length of a unit cell, A is the cross-sectional area of the system, and

$$k_{\pm}^2 \equiv \frac{(E \pm i\gamma)^2 - \Delta^2}{(\hbar v)^2}, \quad \text{Im} k_{\pm} > 0. \quad (43)$$

For an SWCNT, A is conventionally taken to be $A \equiv \pi d_t \delta$, where $\delta = 0.34$ nm is the van der Waals diameter of carbon.

Figures 1(a) and 1(b) show $\rho(E)$ near the band gap of (10,0) SWCNTs per spin and orbital for $\tau = 10, 30, 50$, and 100 fs ($\gamma = 32.91, 10.97, 6.58$, and 3.29 meV) calculated using Eq. (41) and the corresponding semi-log plots, respectively. Two sharp peaks of $\rho(E)$ appear around $E = \pm\Delta = \pm 0.475$ eV, corresponding to the van Hove singularity points of pristine (10,0) SWCNTs without disorder. The maximum value of $\rho(E)$ decreases with decreasing τ (increasing γ) due to disorder scattering. In the high-energy region of $|E| \gg \Delta$, the

$\rho(E)$ data in Figs. 1(a) and 1(b) converge to the constant value of $\rho(\infty) = a/\pi\hbar v = 0.206/\text{eV}$, which is independent of τ , where the unit cell length a of a (10,0) SWCNT is $a = 0.426$ nm and the velocity v of a Dirac electron in the (10,0) SWCNT is given by $v = 1.027 \times 10^6$ m/s. In addition, a (10,0) SWCNT with finite τ exhibits a finite DOS even in its band gap ($|E| < \Delta$), which increases with decreasing τ (increasing γ), as shown in Fig. 1(b). As shown below, the in-gap states have a crucial consequence in the thermoelectric effects of SWCNTs.

Figures 2(a) and 2(b) show the spectral conductivities of (10,0) SWCNTs for $\tau = 10, 30, 50$, and 100 fs calculated using Eq. (42) and the corresponding semi-log plots, respectively. Here, $\alpha(E)$ in Eq. (42) was multiplied by a factor of 4 for the (10,0) SWCNTs because their lowest-conduction (LC) and highest-valence (HV) bands both have two-fold orbital degeneracy and two-fold spin degeneracy (see Appendix A). It can be seen that $\alpha(E)$ in $|E| > \Delta$ decreases with decreasing τ , whereas that in $|E| < \Delta$ increases with decreasing τ (Fig. 2(b)) because the DOS of the in-gap states increases with increasing τ , as shown in Fig. 1(b). Once $\alpha(E)$ is obtained, the electrical conductivity L_{11} and thermoelectrical conductivity L_{12} can be respectively calculated using Eqs. (38) and (35), and then the Seebeck coefficient S and the power factor PF can be respectively obtained using Eqs. (15) and (16).

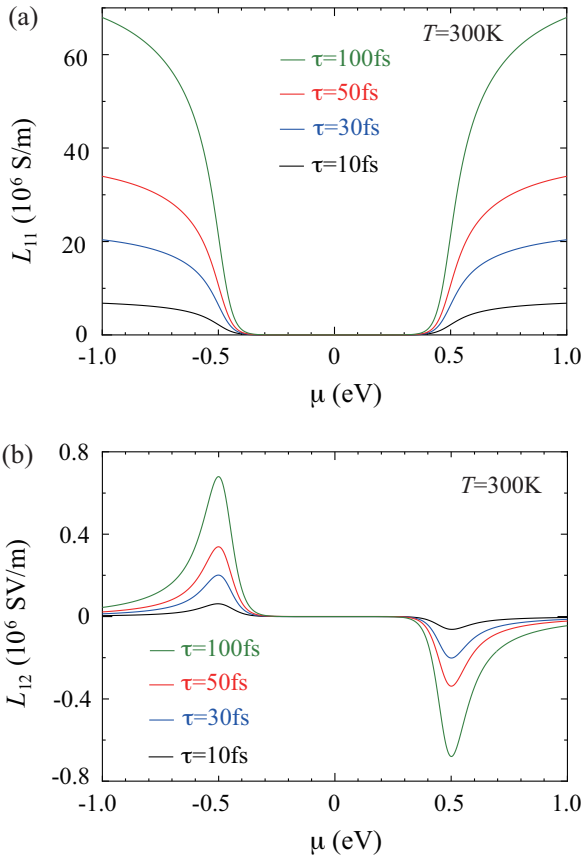


Fig. 3. (Color online) Chemical potential dependence of (a) electrical conductivity L_{11} and (b) thermoelectric conductivity L_{12} of (10,0) SWCNTs for $\tau = 10$ (black curve), 30 (blue curve), 50 (red curve), and 100 fs (green curve) calculated using the constant- τ approximation.

3.1.2 Chemical potential dependence of L_{11} and L_{12} at 300 K

Inspired by recent experiments regarding the bipolar thermoelectric effects of SWCNTs using the FET setup,¹²⁾ we study the μ dependence of L_{11} and L_{12} of SWCNTs at $T = 300$ K. Figure 3(a) shows the μ dependence of the L_{11} of (10,0) SWCNTs for $\tau = 10, 30, 50,$ and 100 fs at $T = 300$ K. As expected from Eq. (38), the μ dependence of L_{11} for each τ value shows features similar to those of the spectral conductivity $\alpha(E)$ in Fig. 2(a). As shown in Fig. 3(b), the L_{12} values of (10,0) SWCNTs for $\tau = 10, 30, 50,$ and 100 fs at $T = 300$ K have a sharp dip or peak near the conduction and valence band edges ($E = \pm\Delta$), respectively.

3.1.3 Chemical potential dependence of S and PF at 300 K

By substituting the L_{11} and L_{12} data in Fig. 3 into Eq. (15), the μ dependence of the Seebeck coefficient S of (10,0) SWCNTs can be obtained. As shown in Fig. 4(a), the absolute value of S decreases with decreasing τ . In addition, S exhibits a sign inversion from positive (p-type) to negative (n-type) when μ changes from negative to positive. Such a bipolar thermoelectric effect of SWCNTs was recently observed in experiments using an electric double layer transistor.^{12,13)} Moreover, Fig. 4(a) shows that S has maximum and minimum values at the optimal chemical potentials $\mu = \pm\mu_{\text{opt}}$, and that μ_{opt} shifts toward the energy band edge with decreasing τ . This trend is different from that reported in a previous study,

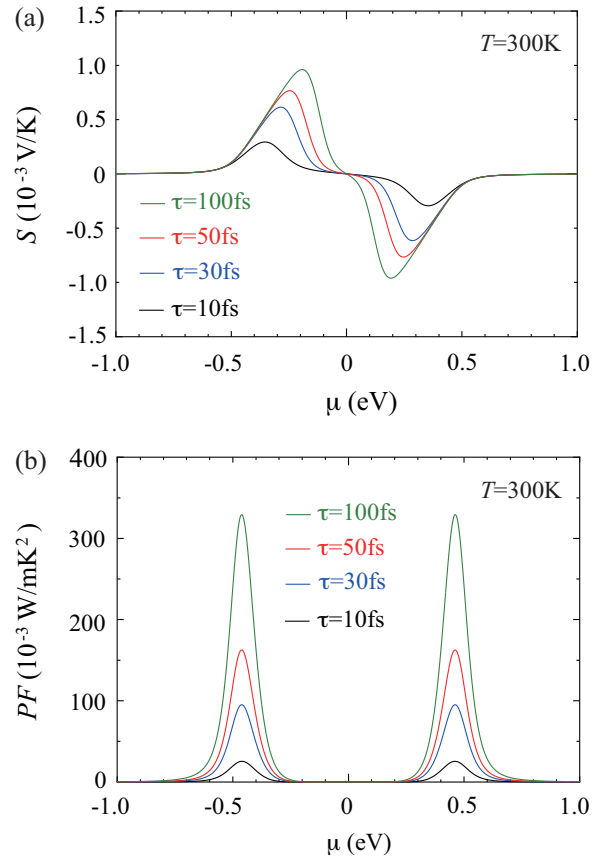


Fig. 4. (Color online) Chemical potential dependence of (a) Seebeck coefficient S and (b) power factor PF of (10,0) SWCNTs for $\tau = 10$ (black curve), 30 (blue curve), 50 (red curve), and 100 fs (green curve) calculated using the constant- τ approximation.

which found that μ_{opt} is independent of τ using the Boltzmann transport theory combined with a model of two independent bands (TIBs) under the constant- τ approximation.¹⁴⁾ The τ -dependent shift of μ_{opt} results from the in-gap states (see Fig. 1(b)), which are not taken into account in the framework of the TIB model.

The power factor PF of (10,0) SWCNTs can also be calculated by substituting the L_{11} and L_{12} data in Fig. 3 into Eq. (16). Figure 4(b) shows the μ dependence of the PF of (10,0) SWCNTs for $\tau = 10, 30, 50,$ and 100 fs at $T = 300$ K. PF has its maximum value near the conduction and valence band edges $E = \pm\Delta (= \pm 0.475 \text{ eV})$ of a pristine (10,0) SWCNT, and decreases with decreasing τ . The high PF , on the order of 100 mW/mK^2 , at the energy band edges is consistent with our previous theoretical work on the μ dependence of the PF of impurity-doped SWCNTs using a single-band approximation.²⁴⁾

Here, we show S and PF as a function of L_{11} (*i.e.*, the S - L_{11} plot and the PF - L_{11} plot) for (10,0) SWCNTs at $T = 300$ K for $\tau = 10$ (black curve), 30 (blue curve), 50 (red curve), and 100 fs (green curve) in Fig. 5(a) and 5(b).

3.2 Self-consistent Born approximation

In this subsection, another refined approximation, *i.e.*, the self-consistent Born approximation (SCBA), is adopted for self-energy corrections due to a disorder potential. For the disorder potential, a short-range random impurity potential is

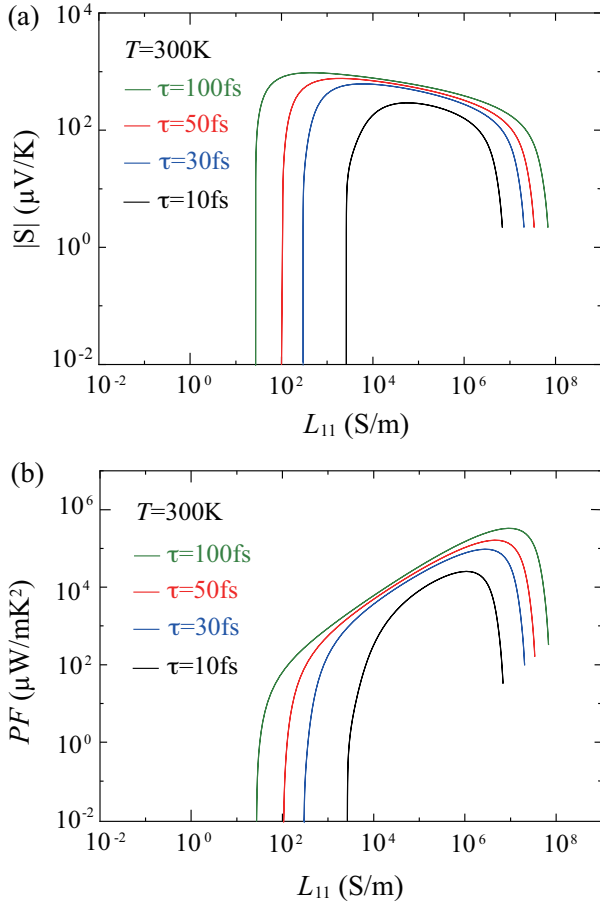


Fig. 5. (a) S - L_{11} plot and (b) PF - L_{11} plot for (10,0) SWCNTs at $T = 300$ K for $\tau = 10$ (black curve), 30 (blue curve), 50 (red curve), and 100 fs (green curve) calculated using the constant- τ approximation.

considered. It includes the following two types of scatterers,

$$U(x) = U_1 a \sum_{\langle j \rangle} \delta(x - x_j) + U_2 a \sum_{\langle l \rangle} \delta(x - x_l), \quad (44)$$

where x_j and x_l represent the locations of different types of impurity, such as n-type and p-type impurities, and $\langle j \rangle$ and $\langle l \rangle$ denote the sums of different impurity sites (*i.e.*, $j \neq l$). The potential strengths U_1 and U_2 are given by

$$U_1 \equiv \begin{pmatrix} u_{11} & 0 \\ 0 & 0 \end{pmatrix} \quad \text{and} \quad U_2 \equiv \begin{pmatrix} 0 & 0 \\ 0 & u_{22} \end{pmatrix}. \quad (45)$$

When the potential is expressed as Eq. (45), the vertex correction vanishes, as shown in Appendix C. In this case, the impurity potential in the momentum space is given by

$$U(q) = \frac{1}{L} \int_{-\infty}^{\infty} dx e^{-iqx} U(x) \quad (46)$$

$$= \frac{U_1}{N} \sum_{\langle j \rangle} e^{-iqx_j} + \frac{U_2}{N} \sum_{\langle l \rangle} e^{-iqx_l}, \quad (47)$$

where N is the total number of unit cells in the system.

In the SCBA for the short-range potential in Eq. (47) with Eq. (45), the retarded self-energy matrix is given in a diagonal and k -independent form as

$$\Sigma^R(E) = \begin{pmatrix} \Sigma_{11}^R(E) & 0 \\ 0 & \Sigma_{22}^R(E) \end{pmatrix}, \quad \text{Im} \Sigma_{jj}^R(E) < 0 \quad (48)$$

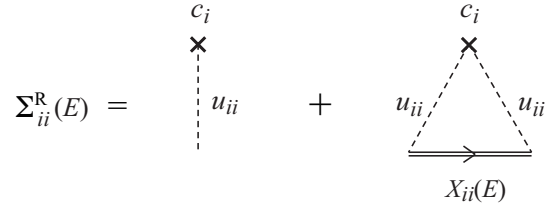


Fig. 6. Self-consistent Born approximation for the retarded self-energy $\Sigma_{ii}^R(E)$ ($i = 1, 2$) of a one-particle retarded Green's function. The \times marks, dotted lines, and solid double lines with an arrow denote the impurity potential, and k -averaged retarded Green's function $X_{ii}(E)$ to be determined self-consistently, respectively.

and the self-consistency equations are

$$\Sigma_{11}^R(E) = c_1 u_{11} + c_1 u_{11}^2 X_{11}(E) \quad (49)$$

$$\Sigma_{22}^R(E) = c_2 u_{22} + c_2 u_{22}^2 X_{22}(E) \quad (50)$$

with $X_{jj}(E) \equiv \frac{1}{N} \sum_k G_{jj}^R(k, E)$ ($j = 1, 2$). In Eqs. (49) and (50), $c_1 \equiv N_1/N$ and $c_2 \equiv N_2/N$ are the concentrations of impurities (*i.e.*, the impurity density per unit cell) with potential strengths u_{11} and u_{22} , respectively (see Fig. 6). Moreover, $X_{11}(E)$ and $X_{22}(E)$ can be analytically calculated for the 1D Dirac electrons as

$$X_{11}(E) = -i \frac{a}{2\hbar v} \frac{\kappa_2}{\sqrt{\kappa_1 \kappa_2}}, \quad (51)$$

$$X_{22}(E) = -i \frac{a}{2\hbar v} \frac{\kappa_1}{\sqrt{\kappa_1 \kappa_2}} \quad (52)$$

with $\kappa_1 \equiv (E - \Delta - \Sigma_{11}^R(E))/\hbar v$, $\kappa_2 \equiv (E + \Delta - \Sigma_{22}^R(E))/\hbar v$, and $\text{Im} \sqrt{\kappa_1 \kappa_2} > 0$. Thus, the self-consistent equations for 1D Dirac electrons are given by

$$\Sigma_{11}^R(E) - c_1 u_{11} = -i \frac{\hbar}{2\tau_1} \frac{\kappa_2}{\sqrt{\kappa_1 \kappa_2}}, \quad (53)$$

$$\Sigma_{22}^R(E) - c_2 u_{22} = -i \frac{\hbar}{2\tau_2} \frac{\kappa_1}{\sqrt{\kappa_1 \kappa_2}}, \quad (54)$$

where τ_1 and τ_2 are the relaxation times related to u_{11} and u_{22} in the limit $|E| \rightarrow \infty$, which are defined as $\tau_1 \equiv \frac{\hbar^2 v}{c_1 u_{11}^2 a}$ and $\tau_2 \equiv \frac{\hbar^2 v}{c_2 u_{22}^2 a}$, respectively.

The simultaneous equations in Eqs. (53) and (54) can be rewritten as the following equations with respect to $\sigma_1 \equiv (\Sigma_{11}^R(E) - c_1 u_{11})/\Delta$ and $\sigma_2 \equiv (\Sigma_{22}^R(E) - c_2 u_{22})/\Delta$.

$$\sigma_1^4 - (\epsilon - 1 - c_1 \tilde{u}_{11}) \sigma_1^3 - \eta_1^2 (\epsilon + 1 - c_2 \tilde{u}_{22}) \sigma_1 - \eta_1^3 \eta_2 = 0 \quad (55)$$

and $\sigma_1 \sigma_2 = -\eta_1 \eta_2$ with $\epsilon \equiv E/\Delta$, $\eta_1 \equiv \hbar/(2\Delta\tau_1)$, $\eta_2 \equiv \hbar/(2\Delta\tau_2)$, $\tilde{u}_{11} \equiv u_{11}/\Delta$, and $\tilde{u}_{22} \equiv u_{22}/\Delta$. Equation (55) indicates that for each ϵ , there are four solutions of $\sigma_1(\epsilon)$, respectively: four real ones or two real and two complex ones, the latter leading to finite DOS. In order to clearly show the difference between the two cases, Eq. (55) is rewritten as

$$\epsilon = \frac{\eta_1 x_1^3 + (1 + c_1 \tilde{u}_{11}) x_1^2 - (1 - c_2 \tilde{u}_{22})}{x_1^2 + 1} - \frac{\eta_2}{x_1(x_1^2 + 1)}, \quad (56)$$

with $x_1 \equiv \sigma_1/\eta_1$.

In the special case of $\eta_2 = 0$, Eq. (55) gives a cubic equation with respect to real $x_1 (= \sigma_1/\eta_1)$. Figure 7(a) shows Eq. (56) as a function of real x_1 for $\eta_1 = 0.07$ and $\eta_2 = 0$ for

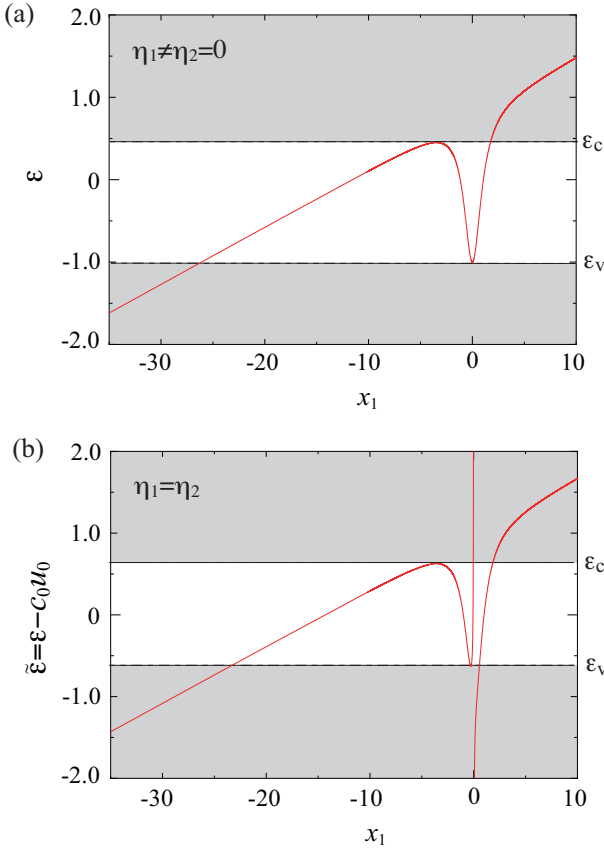


Fig. 7. (Color online) ϵ - x_1 relations for (a) $c_1 = 0.09$, $c_2 = 0$, and $u_{11} = -1.0$ eV (*i.e.*, $\eta_1 = 0.07$ and $\eta_2 = 0$ as well as $\tau_1 = 10$ fs and $\tau_2 = \infty$) and (b) $c_0 (= c_1 = c_2) = 0.09$ and $u_0 (= u_{11} = u_{22}) = -1.0$ eV (*i.e.*, $\eta_1 = \eta_2 = 0.07$ and $\tau_1 = \tau_2 = 10$ fs). The shaded regions indicate the energy regions where the DOS is finite. The broken lines denote the mobility edges ϵ_c and ϵ_v .

(10,0) SWCNTs with $2\Delta = 0.95$ eV. In the shaded regions in Fig. 7(a), Eq. (55) has two complex and one real solutions of x_1 . DOS is finite in these energy regions. The boundaries between the finite- and zero-DOS regions (ϵ_c and ϵ_v in Fig. 7(a)), which are band edges, can be determined using the condition $d\epsilon/dx_1 = 0$. In coherent potential approximation (CPA) methods, including the present SCBA, the spectral conductivity $\alpha(E)$ becomes finite once DOS becomes finite (see § 3.2.1), since CPA ignores the effects of Anderson localization due to the interference effects of scattered waves, which can lead to finite DOS even in the energy region where the conductivity is zero. It is known that every state is localized in one and two dimensions in the presence of finite scattering.³⁵⁾ However, once the system size or temperature becomes finite, the effects of Anderson localization are greatly reduced. This situation is assumed in the present study and hence the band edges in the CPA are used to represent the effective mobility edges. For the case of $\eta_2 = 0$, one of the mobility edges is always $\epsilon_v = -1$ (*i.e.*, $E_v = -\Delta$), as shown in Fig. 7(a).

The case of $c_1 = c_2 (\equiv c_0)$ which we call symmetric case, $\tilde{u}_{11} = \tilde{u}_{22} (\equiv \tilde{u}_0)$ (*i.e.*, $\eta_1 = \eta_2 (\equiv \eta_0)$) is also considered. For this case, Eq. (56) becomes

$$\tilde{\epsilon} = \frac{\eta_0 x_1^3 + x_1^2 - 1}{x_1^2 + 1} - \frac{\eta_0}{x_1(x_1^2 + 1)}, \quad (57)$$

with $\tilde{\epsilon} \equiv \epsilon - c_0 \tilde{u}_0$. Figure 7(b) shows $\tilde{\epsilon}$ in Eq. (57) as a func-

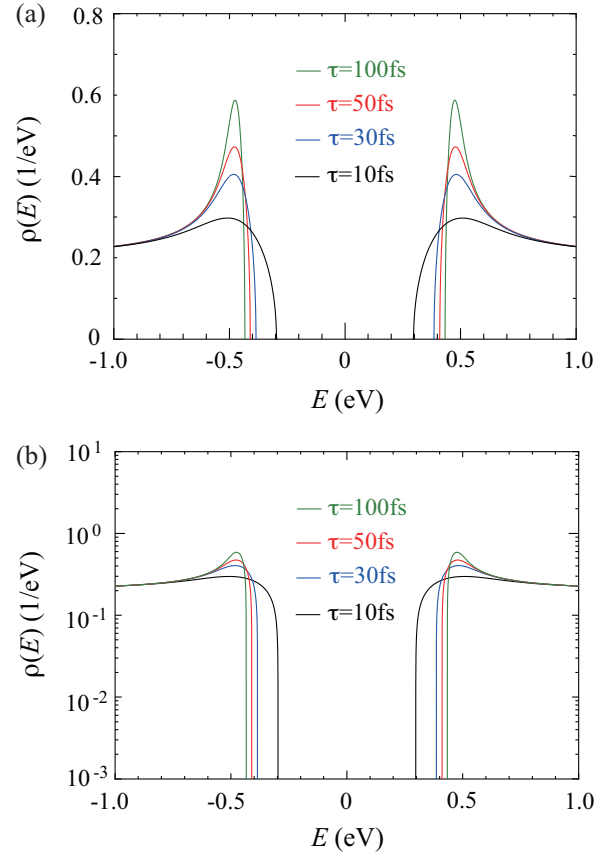


Fig. 8. (Color online) (a) Density of states of the lowest-conduction and the highest-valence bands of (10,0) SWCNTs per spin and orbital for $\tau = 10$ (black curve), 30 (blue curve), 50 (red curve), and 100 fs (green curve) calculated using the SCBA and (b) the corresponding semi-log plots.

tion of real x_1 for $\eta_1 = \eta_2 = 0.07$, corresponding to (10,0) SWCNTs with $2\Delta = 0.95$ eV, and $\tau_1 = \tau_2 = 10$ fs. In the shaded regions in Fig. 7(b), Eq. (55) has two complex and two real solutions of x_1 . These regions have finite DOS. The two mobility edges (ϵ_c and ϵ_v) satisfy $\epsilon_c = -\epsilon_v$, as shown in Fig. 7(b).

The following discussion mainly focuses on thermoelectric properties of SWCNTs for the symmetric case of $\eta_1 = \eta_2$ (*i.e.*, $\tau_1 = \tau_2$). The thermoelectric properties for the asymmetric case of $\eta_1 \neq \eta_2$ will be reported elsewhere.

3.2.1 Density of states and spectral conductivity

Once the self energy $\Sigma^R(E)$ is obtained via the above procedure, the DOS can be calculated using

$$\begin{aligned} \rho(E) &= -\frac{1}{\pi} \sum_{j=1,2} \text{Im} X_{jj}(E) \\ &= \frac{a}{2\pi\hbar v} \text{Re} \left\{ \frac{\kappa_1 + \kappa_2}{\sqrt{\kappa_1 \kappa_2}} \right\}. \end{aligned} \quad (58)$$

Figure 8(a) shows the calculated DOS values near the band gap of (10,0) SWCNTs per spin and orbital for $\tau (\equiv \tau_1 = \tau_2) = 10$ (black curve), 30 (blue curve), 50 (red curve), and 100 fs (green curve) and Fig. 8(b) shows the corresponding semi-log plots. In contrast to the DOS values calculated using the constant- τ approximation (see Fig. 1), clear mobility edges (*i.e.*, E_c and $E_v = -|E_v|$) exist, as shown in Fig. 8. As

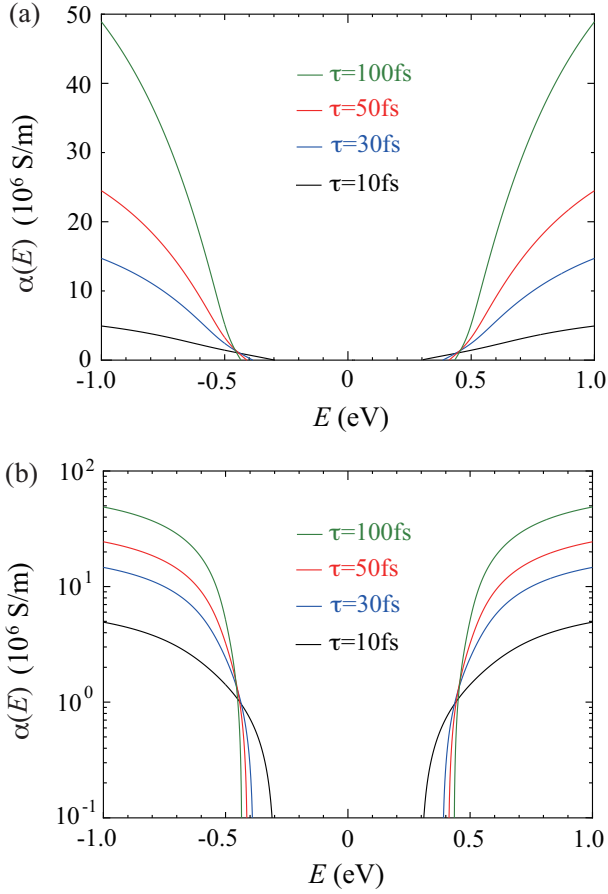


Fig. 9. (Color online) (a) Spectral conductivities of (10,0) SWCNTs for $\tau = 10$ (black curve), 30 (blue curve), 50 (red curve), and 100 fs (green curve) calculated using the SCBA and (b) the corresponding semi-log plots.

τ decreases, the band gap becomes small and the value of the DOS peak decreases. It can also be seen that the DOS near the mobility edges shows the behaviors $\rho(E) \propto \sqrt{E - E_c}$ for $E \geq E_c (> 0)$ and $\rho(E) \propto \sqrt{E_v - E}$ for $E \leq E_v (< 0)$, respectively.

When the self-energy matrix is given in a diagonal and k -independent form, as shown in Eq. (48), the spectral conductivity $\alpha(E)$ in Eq. (36) can be analytically calculated as

$$\alpha(E) = \frac{1}{A} \frac{e^2}{h} \frac{1}{\text{Im}(\kappa_1 \kappa_2)} \text{Re} \left\{ \frac{2\kappa_1 \kappa_2 + \kappa_1^* \kappa_2 + \kappa_1 \kappa_2^*}{\sqrt{\kappa_1 \kappa_2}} \right\} \quad (59)$$

with $\text{Im} \sqrt{\kappa_1 \kappa_2} > 0$. Note that Eq. (59) reduces to Eq. (42) in the constant- τ approximation (*i.e.*, $\Sigma^R = -i\hbar/2\tau$). Figure 9(a) shows the spectral conductivity $\alpha(E)$ of (10,0) SWCNTs for $\tau (\equiv \tau_1 = \tau_2) = 10$ (black curve), 30 (blue curve), 50 (red curve), and 100 fs (green curve) and Fig. 9(b) shows the corresponding semi-log plots. Here, $\alpha(E)$ in Eq. (59) was multiplied by a factor of 4. In contrast to the results obtained with the constant- τ approximation (see Fig. 2), $\alpha(E)$ has a clear gap, as shown in Figs. 9(a) and 9(b). It can also be seen that $\alpha(E)$ near the mobility edges $E = E_c (> 0)$ and $E = E_v (< 0)$ shows the behaviors $\alpha(E) \propto (E - E_c)$ for $E \geq E_c$ and $\alpha(E) \propto (E_v - E)$ for $E \leq E_v$, respectively (see Appendix D for details).

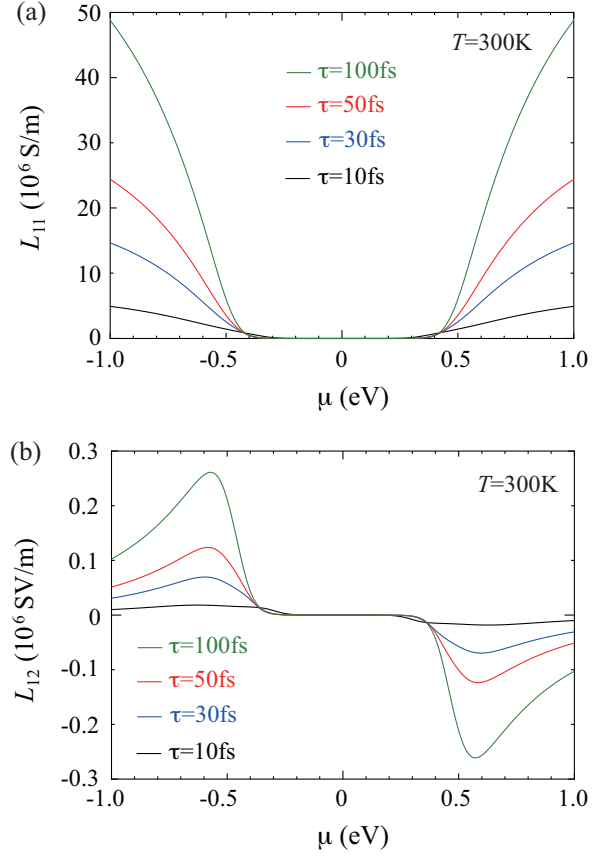


Fig. 10. (Color online) Chemical potential dependence of (a) electrical conductivity L_{11} and (b) thermoelectrical conductivity L_{12} of (10,0) SWCNTs at 300 K for $\tau = 10$ (black curve), 30 (blue curve), 50 (red curve), and 100 fs (green curve) calculated using the SCBA.

3.2.2 Chemical potential dependence of L_{11} and L_{12} at 300 K

Figure 10(a) shows the μ dependence of the L_{11} of (10,0) SWCNTs at 300 K for $\tau (\equiv \tau_1 = \tau_2) = 10$ (black curve), 30 (blue curve), 50 (red curve), and 100 fs (green curve). As expected from Eq. (38), the μ dependence of L_{11} for each τ shows features similar to those for the E dependence of the spectral conductivity $\alpha(E)$ in Fig. (8). As shown in Fig. 10(b), the L_{12} values of (10,0) SWCNTs for $\tau = 10, 30, 50,$ and 100 fs at $T = 300$ K have peaks and dips near the mobility edges ($E = E_c$ and $E_v (= -E_c)$), respectively. These characteristics of L_{11} and L_{12} are essentially the same as those obtained using the constant- τ approximation in the previous section.

3.2.3 Chemical potential dependence of S and PF at 300 K

Figure 11(a) shows the μ dependence of the Seebeck coefficient S of (10,0) SWCNTs for $\tau = 10, 30, 50,$ and 100 fs at 300 K, which was obtained by substituting the L_{11} and L_{12} data in Fig. 10 into Eq. (15). As shown in Fig. 11(a), the absolute value of S decreases with decreasing τ , and S exhibits bipolar effects as a function of μ (*i.e.*, a bipolar thermoelectric effect).^{12,13} In contrast to the results shown in Fig. 4(a), the optimal chemical potentials $\mu = \pm\mu_{\text{opt}}$ are almost independent of τ . Figure 11(b) shows the power factor PF of (10,0) SWCNTs for $\tau = 10, 30, 50,$ and 100 fs at $T = 300$ K, which was calculated by substituting the L_{11} and L_{12} data in Fig. 10 into Eq. (16). Similar to the results obtained using the constant- τ

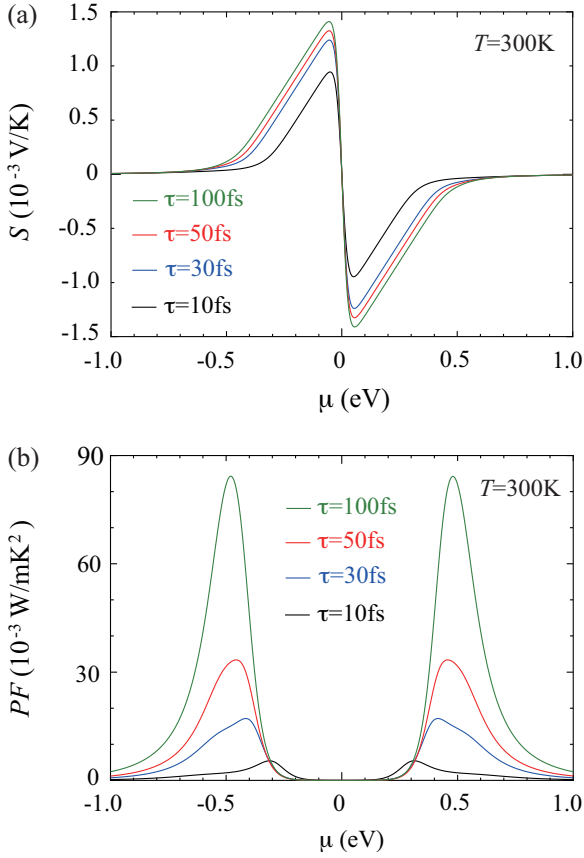


Fig. 11. (Color online) Chemical potential dependence of (a) Seebeck coefficient S and (b) power factor PF of (10,0) SWCNTs at 300 K for $\tau = 10$ (black curve), 30 (blue curve), 50 (red curve), and 100 fs (green curve) calculated using the SCBA.

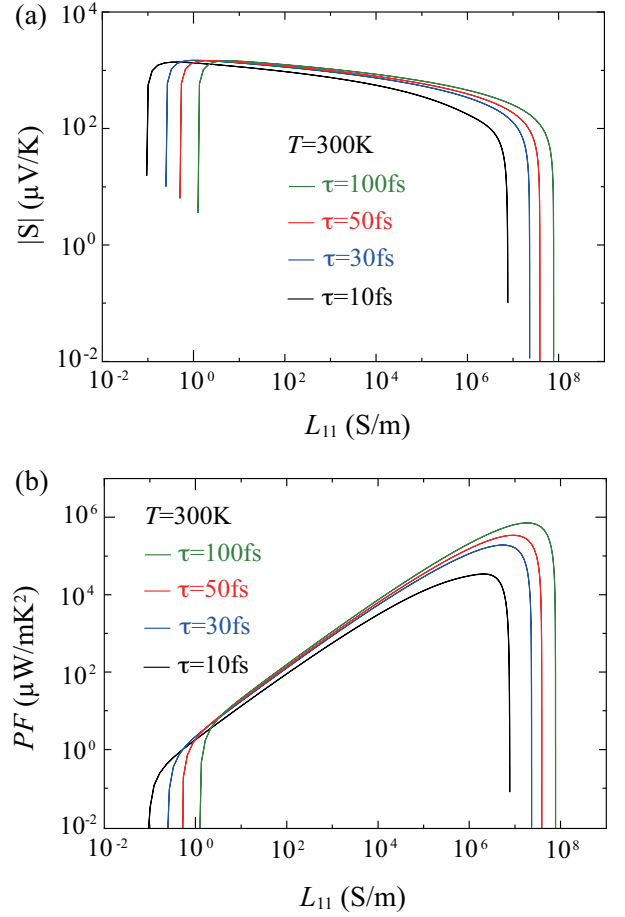


Fig. 12. (a) S - L_{11} plot and (b) PF - L_{11} plot for (10,0) SWCNTs at $T = 300$ K for $\tau = 10$ (black curve), 30 (blue curve), 50 (red curve), and 100 fs (green curve) calculated using the SCBA.

approximation, PF has a maximum value near the conduction and valence band edges of pristine (10,0) SWCNTs.

Here, we show S and PF as a function of L_{11} (*i.e.*, the S - L_{11} plot and the PF - L_{11} plot) for (10,0) SWCNTs at $T = 300$ K for $\tau = 10$ (black curve), 30 (blue curve), 50 (red curve), and 100 fs (green curve) in Fig. 12(a) and 12(b).

3.3 Low-temperature behavior of Seebeck coefficient

In this section, we discuss the low-temperature behavior of S for SWCNTs within SCBA. Since a clear band gap exists, as shown in Fig. 9, the spectral conductivity $\alpha(E)$ can be divided into two parts as

$$\alpha(E) = \alpha_c(E)\theta(E - E_c) + \alpha_h(E)\theta(E - E_v), \quad (60)$$

where $\alpha_{e(h)}(E)$ is the conduction-electron (valence-hole) spectral conductivity and $\theta(x)$ is the Heaviside step function. For this case, the Seebeck coefficient S can be rewritten as

$$S(E) = \frac{1}{T} \frac{L_{12}^e + L_{12}^h}{L_{11}^e + L_{11}^h} = \frac{L_{11}^e S^e + L_{11}^h S^h}{L_{11}^e + L_{11}^h} \quad (61)$$

with

$$L_{11}^e \equiv \int_{E_c}^{\infty} dE \left(-\frac{\partial f(E - \mu)}{\partial E} \right) \alpha_c(E) \quad (62)$$

$$L_{11}^h \equiv \int_{-\infty}^{E_v} dE \left(-\frac{\partial f(E - \mu)}{\partial E} \right) \alpha_h(E) \quad (63)$$

$$L_{12}^e \equiv -\frac{1}{e} \int_{E_c}^{\infty} dE \left(-\frac{\partial f(E - \mu)}{\partial E} \right) (E - \mu) \alpha_c(E) \quad (64)$$

$$L_{12}^h \equiv -\frac{1}{e} \int_{-\infty}^{E_v} dE \left(-\frac{\partial f(E - \mu)}{\partial E} \right) (E - \mu) \alpha_h(E) \quad (65)$$

and $S^{e(h)} \equiv L_{12}^{e(h)} / T L_{11}^{e(h)}$. Here, the superscripts *e* and *h* represent electrons and holes, respectively. Note that although Eq. (61) is formally the same as the TIB model for the Seebeck coefficient based on the Boltzmann transport theory, Eqs. (63)-(65) include the effects of inter-band scattering between the conduction and valence bands, which is not taken into account in TIB model.

The temperature dependence of the Seebeck coefficient for a symmetric case satisfying $E_v = -E_c = \Delta$ is now discussed. For the case of $\mu > E_c$ and $2\Delta \gg k_B T$, L_{11}^h and L_{12}^h can be neglected and $S \approx S^e$. For this case, S^e in the low-temperature limit can be easily obtained as

$$S^e \approx -\frac{\pi^2 k_B^2 T}{3e} \left(\frac{d \ln \alpha_c(E)}{dE} \right)_{E=\mu}, \quad (\mu > E_c) \quad (66)$$

by performing the Sommerfeld expansion of Eqs. (63)-(65). The T -linear behavior of S , known as Mott's formula,³⁹ can be seen for the (10,0) SWCNTs when μ is larger than $E_c = 0.30$ eV, as shown in Fig. 13. The T -linear region becomes smaller as μ approaches the mobility edge E_c .

When $\mu = E_c$, the above-mentioned T -linear region van-

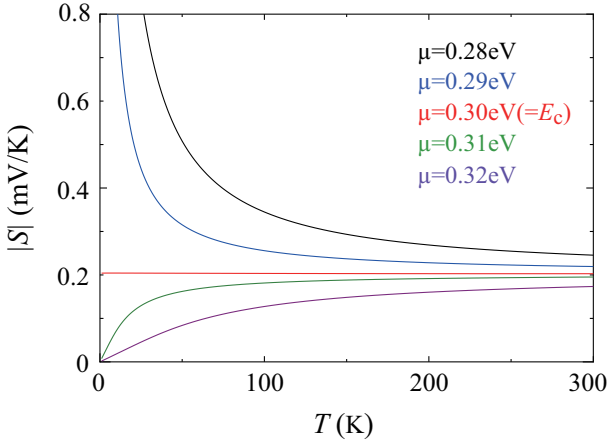


Fig. 13. (Color online) Temperature dependence of the Seebeck coefficient of (10,0) SWCNTs with $\tau = 10$ fs for $\mu = 0.28$ eV (black curve), 0.29 eV (blue curve), 0.30 eV ($= E_c$) (red curve), 0.31 eV (green curve), and 0.32 eV (purple curve). Here, E_c is the mobility edge.

ishes and S^e becomes constant as

$$S^e = \frac{k_B}{e} \frac{\int_0^\infty dx \left(-\frac{\partial f(x)}{\partial x} \right) x^2}{\int_0^\infty dx \left(-\frac{\partial f(x)}{\partial x} \right) x} \approx \frac{k_B}{e} \times 2.37, \quad (\mu = E_c), \quad (67)$$

where $f(x) = 1/(1 + e^x)$ with $x \equiv E - E_c$. For $\mu = E_c (= 0.30$ eV), the Seebeck coefficient S of (10,0) SWCNTs with $\tau = 10$ fs is constant with respect to T , as shown in Fig. 13.

When $\mu < E_c$ but as far as $E_c - \mu \ll 2\Delta$ together with at low temperature $k_B T \ll E_c - \mu$, the valence holes are frozen out (*i.e.*, $L_{11}^h = 0$ and $L_{12}^h = 0$) and the Seebeck coefficient $S \approx S^e$, which is inversely proportional to T as

$$S^e \approx -S_0 - \frac{E_c - \mu}{eT}, \quad (\mu < E_c; k_B T \ll E_c - \mu \ll 2\Delta). \quad (68)$$

with

$$S_0 = \frac{k_B}{e} \frac{\int_0^\infty dx e^x x^2}{\int_0^\infty dx e^x x} = \frac{2k_B}{e}. \quad (69)$$

Here, we note $f(E - \mu) \approx e^{-(E-\mu)/k_B T}$ for $E > E_c$ and $\alpha(E) \propto (E - E_c)$ near $E = E_c$. The T^{-1} behavior of S can be seen for (10,0) SWCNTs with $\tau = 10$ fs for $\mu = 0.28$ eV and 0.29 eV ($< E_c = 0.30$ eV) in Fig. 13.

4. Comparison with experiments

As shown in Figs. 4(a) and 11(a), the present theory naturally leads to the bipolar thermoelectric effects of SWCNTs, *i.e.*, the sign inversion of the Seebeck coefficient from positive (p-type) to negative (n-type) when the chemical potential is changed at room temperature as observed in experiments.^{12,13)}

Regarding the tradeoff relation between S and L_{11} for SWCNTs at room temperature *i.e.*, decreasing S with increasing L_{11} as seen in experiment²¹⁾ would be understood by our theoretical results in Fig. 5 and Fig. 12. It is to be noted that the S - L_{11} tradeoff relation changes when μ is located near the middle of the band gap, which can be observed in experiments using the FET setup. This tradeoff between S and L_{11} would be naturally reflected in between PF and L_{11} as indicated in Fig. 5(b) and Fig. 12(b).

In addition, the crossover from T -linear to T -inverse be-

havior of the Seebeck coefficient at low temperature in Fig. 13 will also be an interesting experimental challenge.

5. Conclusion

The present study based on 1D Dirac electrons has developed a theoretical framework of bipolar thermoelectric effects in SWCNT described as 1d Dirac electrons under disorder. Based on the thermal Green's functions, effects of disorder have been treated within self-consistent Born approximation (SCBA), which is the simplest version of coherent potential approximation (CPA). The results has led to prediction of characteristic behaviors of Seebeck coefficient and power factor of semiconducting SWCNT, including the sign change of Seebeck coefficient as a function of chemical potential (gate voltage) as observed in recent experiments.^{12,13)} It is to be noted that the effects of Anderson localization, which will play important roles at low temperatures, are totally ignored in the present study since our interest here in mainly at elevated temperatures, *e.g.*, room temperature. We have also studied the crossover from T -linear to T -inverse behavior of the Seebeck coefficient of semiconducting SWCNTs at low T when the chemical potential changes from $\mu > E_c$ to $\mu < E_c$. The $S \propto 1/T$ behavior for $\mu < E_c$, which is commonly seen in text books,^{40,41)} should be taken with care for the temperature range of its observability because the present linear response theory breaks down in the limit of $T \rightarrow 0$,⁴²⁾ which needs separate and detailed studies.

The authors would like to thank Masao Ogata, Hiroyasu Matsuura, Hideaki Maehashi, Satoru Konabe, and Kenji Sasaoka for valuable discussions, and also Kazuhiro Yanagi for providing experimental data on the thermoelectric effects of carbon nanotubes. This work was supported, in part, by a JSPS KAKENHI grant (no. 15H03523).

Appendix A: 1D Dirac electrons in semiconducting carbon nanotubes

Figures A-1(a) and A-1(b) show the real and reciprocal lattices of graphene, respectively. The two-dimensional principal lattice vectors are $\mathbf{a}_1 = (-\sqrt{3}a/2, a/2)$ and $\mathbf{a}_2 = (\sqrt{3}a/2, a/2)$ with $a \equiv |\mathbf{a}_1| = |\mathbf{a}_2| = 0.246$ nm. The unit cell contains two carbon atoms, A and B. The reciprocal lattice vectors are $\mathbf{b} = (-2\pi/\sqrt{3}a, 2\pi/a)$ and $\mathbf{b}_2 = (2\pi/\sqrt{3}a, 2\pi/a)$, respectively. In particular, the Γ , K, and K' points of the Brillouin zone are given by $\Gamma = (0, 0)$, K = $(4\pi/\sqrt{3}a, 0)$, and K' = $(2\pi/\sqrt{3}a, 2\pi/a)$, respectively.

The π -orbital tight-binding Hamiltonian of graphene is given by

$$H(\mathbf{k}) = \begin{pmatrix} 0 & H_{AB}(\mathbf{k}) \\ H_{BA}(\mathbf{k}) & 0 \end{pmatrix}, \quad (A-1)$$

with the matrix elements $H_{AB}(\mathbf{k}) = (H_{BA}(\mathbf{k}))^*$, which are given by

$$\begin{aligned} H_{AB}(\mathbf{k}) &\equiv -\gamma_0 \sum_{l=1}^3 e^{i\mathbf{k} \cdot \mathbf{R}_l} \\ &= -\gamma_0 \left(e^{i\mathbf{k}_x a / \sqrt{3}} + 2e^{-i\mathbf{k}_x a / 2\sqrt{3}} \cos \frac{\mathbf{k}_y a}{2} \right). \end{aligned} \quad (A-2)$$

Here, $\mathbf{R}_1 = (a/\sqrt{3}, 0)$, $\mathbf{R}_2 = (-a/2\sqrt{3}, a/2)$, and $\mathbf{R}_3 = (-a/2\sqrt{3}, -a/2)$ are the vectors going from a B lattice point to three neighboring A lattice points, as shown in Fig. A-1. γ_0 is

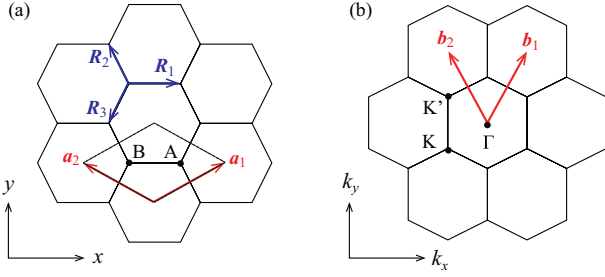


Fig. A-1. (a) Lattice structure of graphene and two primitive translation vectors given by \mathbf{a}_1 and \mathbf{a}_2 . The unit cell is described by a hexagon containing two carbon atoms, A and B. \mathbf{R}_j ($j = 1, 2, 3$) are three vectors directed from a B atom to the three nearest neighbor A atoms. (b) Reciprocal lattice of graphene. \mathbf{b}_1 and \mathbf{b}_2 are the reciprocal lattice vectors. The center of the hexagon (the first Brillouin zone) is called the Γ point and the vertices of the hexagon are called K and K' points.

the hopping integral between nearest-neighbor carbon atoms (π orbitals, set to $\gamma_0 = 2.7\text{eV}$ in the present study). By diagonalizing the Hamiltonian in Eq. (A-5), the energy dispersion relation of graphene can be obtained as

$$E_{\pm}(\mathbf{k}) = \pm\gamma_0 \sqrt{1 + 4\cos\frac{\sqrt{3}ak_x}{2} \cos\frac{ak_y}{2} + 4\cos^2\frac{ak_y}{2}} \quad (\text{A-4})$$

with the gapless points (so-called Dirac points) at the K and K' points. In Eq. (A-4), the sign \pm represents the conduction (+) and valence (−) bands, respectively. As is well known, graphene has the linear dispersion relation $E_{\pm}(\mathbf{k}) \approx \pm\hbar v|\mathbf{k}|$ with $v = \sqrt{3}a\gamma_0/2\hbar$ around the K and K' points.

Here, zigzag-edged SWCNTs (z-SWCNTs) are considered as an example of pure 1D semiconductors. The Hamiltonian of a z-SWCNT can be obtained by imposing the periodic boundary condition along the y axis to the graphene as follows.

$$H_q(k) = \begin{pmatrix} 0 & H_{AB}^{(q)}(k) \\ H_{BA}^{(q)}(k) & 0 \end{pmatrix} \quad (\text{A-5})$$

with the matrix elements $H_{AB}^{(q)}(k) = (H_{BA}^{(q)}(k))^*$,

$$H_{AB}^{(q)}(k) = -\gamma_0 e^{ika/\sqrt{3}} \left(1 + 2e^{-i\sqrt{3}ak/2} \cos\frac{\pi q}{n} \right), \quad (\text{A-6})$$

where k is the wavenumber along the tube-axial direction, $q = 0, 1, \dots, 2n-1$ is the discrete wavenumber along the circumferential direction, and n is a natural number ($n = 1, 2, \dots, \infty$) specifying the unique structure of a particular z-SWCNT. Herein, a z-SWCNT with index n is represented as $(n, 0)$ CNT in accordance with customary practice.

The energy dispersion relations $E_{\pm}^{(q)}(k)$ of the conduction (+) and valence (−) bands can be expressed as^{37,38)}

$$E_{\pm}^{(q)}(k) = \pm\gamma_0 \sqrt{1 + 4\cos\left(\frac{ka_z}{2}\right) \cos\left(\frac{q\pi}{n}\right) + 4\cos^2\left(\frac{q\pi}{n}\right)}, \quad (\text{A-7})$$

$$(q = 0, 1, \dots, 2n-1 \quad \text{and} \quad -\pi/a_z < k < \pi/a_z).$$

Here, $a_z = 0.426\text{ nm}$ is the unit cell length of the z-CNTs. A $(n, 0)$ CNT includes $4n$ carbon atoms in the unit cell and its diameter d_t is given by $d_t = \frac{na_z}{\sqrt{3}\pi}$.

z-SWCNTs can be either metallic or semiconducting depending on whether or not n is a multiple of 3, respectively.

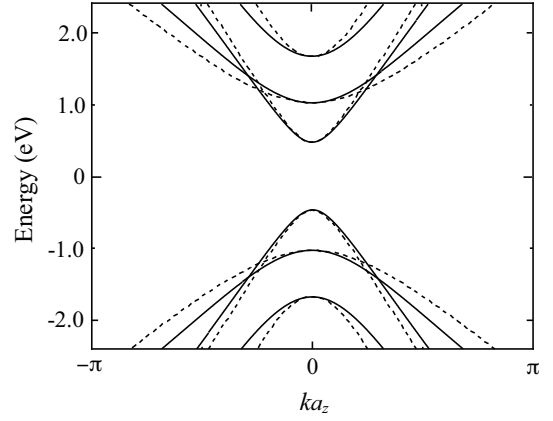


Fig. A-2. Energy bands around the Fermi energy ($\epsilon_F = 0\text{ eV}$) of a $(10,0)$ z-SWCNT calculated using the π -orbital tight-binding model (solid curves) and the 1D Dirac electron model (dashed curves). Each curve is two-fold degenerate. The lowest conduction bands and the highest valence bands are denoted as the discrete wavenumber $(q_1, q_2) = (7, 10)$ along the circumferential direction of the $(10,0)$ z-SWCNT, respectively. Similarly, the 2nd-lowest conduction bands and the 2nd-highest valence bands are denoted $(q_1, q_2) = (6, 14)$, and the 3rd-lowest conduction bands and the 3rd-highest valence bands are denoted as $(q_1, q_2) = (8, 12)$.

For the case of metallic z-SWCNTs ($n \bmod 3 = 0$), two pairs of lowest-conduction (LC) and highest-valence (HV) bands $E_{\pm}^{(q)}(k)$ are specified by the following two values of q , respectively.

$$q = \begin{cases} q_1 \equiv 2n/3 \\ q_2 \equiv 4n/3 \end{cases} \quad \text{for } n \bmod 3 = 0. \quad (\text{A-8})$$

For the case of semiconducting z-SWCNTs ($n \bmod 3 \neq 0$), the two pairs of LC and HV bands are respectively specified by

$$q = \begin{cases} q_1 \equiv (2n+1)/3 \\ q_2 \equiv (4n-1)/3 \end{cases} \quad \text{for } n \bmod 3 = 1 \quad (\text{A-9})$$

and

$$q = \begin{cases} q_1 \equiv (2n-1)/3 \\ q_2 \equiv (4n+1)/3 \end{cases} \quad \text{for } n \bmod 3 = 2. \quad (\text{A-10})$$

As can be seen in Eqs. (A-8)-(A-10), both the LC and HV bands will have two-fold degeneracy (q_1 and q_2) for a given n .

In the long-wavelength limit ($k \rightarrow 0$), the Hamiltonian matrix of z-SWCNT in Eq. (A-6) can be approximately expressed as

$$H_{AB}^{(q)}(k) \approx e^{i\theta_k} \left\{ \left(\Delta_q + \frac{\hbar^2 k^2}{2m_q} \right) + i\hbar v_q k \right\} \quad (\text{A-11})$$

with $\theta_k = ka/\sqrt{3}$ and

$$\Delta_q = -\gamma_0 \left\{ 1 + 2\cos\frac{\pi q}{n} \right\} \quad (\text{A-12})$$

$$m_q^{-1} = \frac{a_z^2 \gamma_0}{2\hbar^2} \cos\frac{\pi q}{n} \quad (\text{A-13})$$

$$v_q = \frac{a_z \gamma_0}{\hbar} \cos\frac{\pi q}{n}. \quad (\text{A-14})$$

The unitary transform of the Hamiltonian in Eq. (A-17) can

now be performed as

$$\tilde{H}_q(k) \equiv U_k^\dagger H_q(k) U_k \quad (\text{A}\cdot 15)$$

$$= \begin{pmatrix} \Delta_q + \frac{\hbar^2 k^2}{2m_q} & \hbar v_q k \\ \hbar v_q k & -\Delta_q - \frac{\hbar^2 k^2}{2m_q} \end{pmatrix} \quad (\text{A}\cdot 16)$$

using the unitary matrix

$$U_k = \frac{1}{\sqrt{2}} \begin{pmatrix} 1 & i \\ e^{-i\theta_k} & -ie^{-i\theta_k} \end{pmatrix}. \quad (\text{A}\cdot 17)$$

For the case of $\hbar|k| \ll 2\sqrt{m_q\Delta_q}$ (small wavenumber) and $\Delta_q/m_q v_q^2 \ll 1$ (small band gap), the effective Hamiltonian in Eq. (A·16) can be approximately described by

$$\tilde{H}_q(k) \approx \begin{pmatrix} \Delta_q & \hbar v_q k \\ \hbar v_q k & -\Delta_q \end{pmatrix}. \quad (\text{A}\cdot 18)$$

By diagonalizing the Hamiltonian $\tilde{H}_q(k)$ in Eq. (A·18), the energy dispersion relations $E_k^{(\pm)}$ of the conduction (+) and valence (-) bands of 1D Dirac electrons can be obtained as

$$E_{\pm}^{(q)}(k) = \pm \sqrt{\Delta_q^2 + (\hbar v_q k)^2}. \quad (\text{A}\cdot 19)$$

As an example, Fig. A·2 shows the energy bands $E_{\pm}^{(q)}$ of the (10,0) z-SWCNT calculated using the π -orbital tight-binding model (solid curves) and the 1D Dirac electron model (dashed curves). The dashed curves are in excellent agreement with the solid curve in the vicinity of $k = 0$. For a (10, 0) z-SWCNT, the energy difference ΔE between the bottom of the LC band and the second-lowest conduction band is $\Delta E = 0.557$ eV. Herein, the focus is on the low-energy excitation regime, in which the thermal energy $k_B T$ is much lower than ΔE . In the low-energy excitation regime, the thermoelectric properties of z-SWCNTs can be explained in terms of single-band 1D Dirac electrons in the LC and HV bands denoted as $q = q_1, q_2$ in Eqs. (A·9) and (A·10). Here, it is assumed that the effects of possible mixing between the two LC bands due to impurity scattering can be ignored. This assumption is valid under the condition that the characteristic momentum contributing to the formation of the bound state due to impurity potential is much smaller than the momentum difference between the two LC (HV) bands with $q = q_1$ and q_2 , as discussed in our previous work.²⁴⁾ Thus, in the main text of the present study, the focus is only on the LC and HV bands and the subscript or subscript $q = q_1$ and q_2 is dropped from the 1D Dirac Hamiltonian $h_0(k)$ in Eq. (11).

Appendix B: Derivation of Eq. (24)

This appendix derives Eq. (24). By substituting Eq. (23) into Eq. (22), the energy current J_Q can be rewritten as

$$J_Q = \int_{-\infty}^{\infty} dx \left\{ \frac{\partial \Psi^\dagger(x, t)}{\partial t} \left(\frac{\sin Qx}{2Q} H(x) \right) \Psi(x, t) + \Psi^\dagger(x, t) \left(\frac{\sin Qx}{2Q} H(x) \right) \frac{\partial \Psi(x, t)}{\partial t} \right\} + \text{H.c.} \quad (\text{B}\cdot 1)$$

Applying Eqs. (5) and (6) to Eq. (B·1), J_Q becomes

$$J_Q = \frac{i}{\hbar} \int_{-\infty}^{\infty} dx \frac{\sin Qx}{2Q} \left\{ (H(x)\Psi(x, t))^\dagger (H(x)\Psi(x, t)) - (\Psi^\dagger(x, t)H(x))(H(x)\Psi(x, t)) \right\} + \text{H.c.} \quad (\text{B}\cdot 2)$$

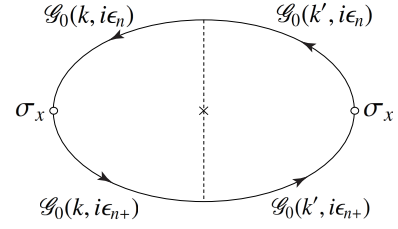


Fig. C·1. Diagram for the correlation function $\chi_{12}(i\omega_\lambda)$ in Eq. (31) with the lowest-order vertex correction. The dashed line with a cross represents an impurity potential U , the solid curves denote the unperturbed thermal Green's functions \mathcal{G}_0 of 1D Dirac electrons, and the circles are the x -component of the Pauli matrix σ_x .

As the 1D Dirac Hamiltonian with a disorder potential $U(x)$ is given by $H(x) = -i\hbar\sigma_x \frac{\partial}{\partial x} + \Delta\sigma_z + U(x)$ in Eq. (2), Eq. (B·2) can be rewritten as

$$J_Q = v \int_{-\infty}^{\infty} dx \frac{\sin Qx}{2Q} \left\{ \frac{\partial \Psi^\dagger(x, t)}{\partial x} \sigma_x H(x) \Psi(x, t) + \Psi^\dagger(x, t) \sigma_x \frac{\partial (H(x)\Psi(x, t))}{\partial x} \right\} + \text{H.c.} \\ = v \int_{-\infty}^{\infty} dx \frac{\cos Qx}{2} \Psi^\dagger(x, t) \sigma_x H(x) \Psi(x, t) + \text{H.c.} \quad (\text{B}\cdot 3)$$

In the limit of $Q \rightarrow 0$, Eq. (24) in the main text can be obtained as

$$J_Q = \frac{v}{2} \int_{-\infty}^{\infty} dx \Psi^\dagger(x, t) (\sigma_x H(x) + H(x) \sigma_x) \Psi(x, t). \quad (\text{B}\cdot 4)$$

Recently, Ogata and Fukuyama gave a general expression of Eq. (24) for multi-band disorder systems based on the Luttinger-Kohn representation.³⁰⁾

Appendix C: Absence of vertex correction

In this appendix, a vertex correction for the current operator. Up to the lowest order of U , $\sigma'_x(k)$ in Eq. (32) is expressed as

$$\sigma'_x(k) = \langle U(k-k') \mathcal{G}_0(k, i\epsilon_{n+}) \sigma_x \mathcal{G}_0(k', i\epsilon_n) U(k'-k) \rangle_{\text{imp}} \quad (\text{C}\cdot 1)$$

where we used $\mathcal{G}(k, k', i\epsilon_n) \approx \delta_{k,k'} \mathcal{G}_0(k, i\epsilon_n)$. We now assume that the impurity potential is a short range and diagonal, that is, $U(q)$ is given by

$$U(q) = \frac{U_0}{N} \sum_{\langle l \rangle} e^{-iqx_l} \quad (\text{C}\cdot 2)$$

with $U_0 = (u_0 I + u_z \sigma_z)$, where I is the 2×2 identity matrix. In this case, $\sigma'_x(k)$ is rewritten as

$$\sigma'_x(k) = \sum_k (U_0 \mathcal{G}_0(k, i\epsilon_{n+}) \sigma_x \mathcal{G}_0(k', i\epsilon_n) U_0) f(k-k') \quad (\text{C}\cdot 3)$$

where $f(q) \equiv \left\langle \left(\frac{1}{N} \sum_{\langle j \rangle} e^{iqx_j} \right) \left(\frac{1}{N} \sum_{\langle l \rangle} e^{-iqx_l} \right) \right\rangle_{\text{imp}}$. Thus, the vertex correction Γ for the correlation function in Eq. (31) is given by

$$\Gamma \propto \sum_{k, k'} \mathcal{G}_0(k, i\epsilon_{n+}) \sigma_x \mathcal{G}_0(k, i\epsilon_n) U \mathcal{G}_0(k', i\epsilon_{n+}) \sigma_x \mathcal{G}_0(k', i\epsilon_n) U \\ = \sum_k \frac{(A(k) \sigma_x - i\omega_\lambda \Delta \sigma_y) (u_0 I + u_z \sigma_z)}{D(k, i\epsilon_{n+}) D(k, i\epsilon_n)}$$

$$\times \sum_{k'} \frac{(A(k')\sigma_x - i\omega_\lambda \Delta \sigma_y)(u_0 I + u_z \sigma_z)}{D(k', i\epsilon_{n+})D(k', i\epsilon_n)} \quad (\text{C}\cdot 4)$$

where $A(k) \equiv i\epsilon_{n+}i\epsilon_n + \Delta^2 + (\hbar v k)^2$. The scattering process in Eq. (C·4) is described in Fig. C·1.

For a 1D Dirac electron, the unperturbed thermal Green's function $\mathcal{G}_0(k, i\epsilon_n)$ of is given by

$$\mathcal{G}_0(k, i\epsilon_n) = \frac{i\epsilon_n + \hbar v k \sigma_x + \Delta \sigma_z}{D(k, i\epsilon_n)}. \quad (\text{C}\cdot 5)$$

with $D(k, i\epsilon_n) \equiv (i\epsilon_n)^2 - (\Delta^2 + (\hbar v k)^2)$ and then the numerator in Eq. (C·4) can be calculated as

$$\begin{aligned} & (A(k)\sigma_x - i\omega_\lambda \Delta \sigma_y)(u_0 I + u_z \sigma_z) \\ & \times (A(k')\sigma_x - i\omega_\lambda \Delta \sigma_y)(u_0 I + u_z \sigma_z) \\ & = \left[(u_0 A(k) + u_z \omega_\lambda \Delta) \sigma_x - i(u_0 \omega_\lambda \Delta + u_z A(k)) \sigma_y \right] \\ & \times \left[(u_0 A(k') + u_z \omega_\lambda \Delta) \sigma_x - i(u_0 \omega_\lambda \Delta + u_z A(k')) \sigma_y \right] \\ & \approx (u_0^2 - u_z^2) [A(k)A(k') - i\omega_\lambda \Delta (A(k) - A(k'))]. \quad (\text{C}\cdot 6) \end{aligned}$$

Thus, the vertex correction in Eq. (C·4) vanishes for $u_z = \pm u_0$, corresponding to the disorder potential in Eq. (45), *i.e.*, the two cases of $u_z = u_0$ and $u_z = -u_0$ correspond to U_1 with $u_{11} = 2u_0$ and U_2 with $u_{22} = 2u_0$, respectively.

Appendix D: Spectral conductivity near the mobility edges

As shown in Eq. (59), the spectral conductivity $\alpha(E)$ is expressed as

$$\alpha(E) \propto \frac{1}{\text{Im}(\kappa_1 \kappa_2)} \text{Re} \left\{ \frac{2\kappa_1 \kappa_2 + \kappa_1^* \kappa_2 + \kappa_1 \kappa_2^*}{\sqrt{\kappa_1 \kappa_2}} \right\} \quad (\text{D}\cdot 1)$$

within the SCBA. In this appendix, it is proven that the spectral conductivity behaves as $\alpha(E) \propto (E - E_c)$ near the mobility edge $E = E_c$.

In the case of $E \lesssim \Delta$, κ_1 and κ_2 are given by

$$\kappa_1 = -\kappa_1^R + i\kappa_1^I, \quad (\text{D}\cdot 2)$$

$$\kappa_2 = \kappa_2^R + i\kappa_2^I \quad (\text{D}\cdot 3)$$

where $\kappa_1^R > 0$ and $\kappa_2^R > 0$. Using these expression, we obtain the following relations.

$$\text{Im}(\kappa_1 \kappa_2) = \kappa_1^I \kappa_2^R - \kappa_1^R \kappa_2^I, \quad (\text{D}\cdot 4)$$

$$\kappa_1^* \kappa_2 + \kappa_1 \kappa_2^* = 2(-\kappa_1^R \kappa_2^R + \kappa_1^I \kappa_2^I), \quad (\text{D}\cdot 5)$$

and

$$\sqrt{\kappa_1 \kappa_2} = i \sqrt{\kappa_1^R \kappa_2^R} (1 + z) \quad (\text{D}\cdot 6)$$

with

$$z \equiv \frac{\kappa_1^I \kappa_2^I}{\kappa_1^R \kappa_2^R} - i \frac{\kappa_1^I \kappa_2^R - \kappa_1^R \kappa_2^I}{\kappa_1^R \kappa_2^R}. \quad (\text{D}\cdot 7)$$

Because of $\kappa_1^I \ll \kappa_1^R$ and $\kappa_2^I \ll \kappa_2^R$ (*i.e.*, $z \ll 1$) near the mobility edge $E = E_c$, Eq. (D·6) near $E = E_c$ can be approximately expressed as

$$\sqrt{\kappa_1 \kappa_2} \approx i \sqrt{\kappa_1^R \kappa_2^R} \left(1 + \frac{z}{2} - \frac{z^2}{8} \right) \quad (\text{D}\cdot 8)$$

and eventually

$$\frac{1}{\sqrt{\kappa_1 \kappa_2}} \approx -i \frac{1}{\sqrt{\kappa_1^R \kappa_2^R}} \left(1 - \frac{z}{2} + \frac{3z^2}{8} \right). \quad (\text{D}\cdot 9)$$

Substituting Eqs. (D·4), (D·5) and (D·9) into Eq. (D·1), we can straightforwardly obtain

$$\alpha(E) \propto \frac{2}{(\kappa_1^R \kappa_2^R)^{3/2}} \kappa_1^I \kappa_2^I \quad (\text{D}\cdot 10)$$

near the mobility edge $E = E_c$. As can be seen in Fig. 8(a) and can be analytically verified from Eq. (56) and Fig. 7 as $\text{Im} \sigma_1 \propto -\sqrt{E - E_c}$ together with $\sigma_1 \sigma_2 = \eta_1 \eta_2$, the DOS is proportional to $\sqrt{E - E_c}$ in the vicinity of $E = E_c$, and κ_1^I and κ_2^I near $E = E_c$ show the behaviors $\kappa_1^I \propto \kappa_2^I \propto \sqrt{E - E_c}$. Therefore, $\alpha(E)$ behaves as

$$\alpha(E) \propto (E - E_c) \quad (\text{D}\cdot 11)$$

near the mobility edge $E = E_c$.

- 1) L.D. Hicks and M. S. Dresselhaus: Phys. Rev. B **47** (1993) 16631.
- 2) Y.-M. Lin, X. Sun and M. S. Dresselhaus: Phys. Rev. B **62** (2000) 4610.
- 3) O. Rabin, Y.-M. Lin and M. S. Dresselhaus: Appl. Phys. Lett. **79** (2001) 81.
- 4) J. P. Heremans, C. M. Thrush, D. T. Morelli, and M. C. Wu: Phys. Rev. Lett. **88** (2002) 216801.
- 5) A.I. Boukai, Y. Bunimovich, J. Tahir-Kheli, J.-K. Yu, W.A. Goddard III, J. R. Heath: Nature **451** (2008) 168.
- 6) A.I. Hochbaum, R. Chen, R.D. Delgado, W. Liang, E.C. Garnett, M. Najarian, A. Majumdar and P. Yang: Nature. **451** (2008) 163.
- 7) J. P. Small, K. M. Perez and P. Kim: Phys. Rev. Lett. **91** (2003) 256801.
- 8) Y. Nakai, K. Honda, K. Yanagi, H. Kataura, T. Kato, T. Yamamoto and Y. Maniwa: Appl. Phys. Express **7** (2014) 025103.
- 9) D. Hayashi, T. Ueda, Y. Nakai, H. Kyakuno, Y. Miyata, T. Yamamoto, T. Saito, K.i Hata and Y. Maniwa: Appl. Phys. Express **9** (2016) 025102.
- 10) D. Hayashi, Y. Nakai, H. Kyakuno, T. Yamamoto, Y. Miyata, K. Yanagi and Y. Maniwa: Appl. Phys. Express **9** (2016) 125103.
- 11) A. D. Avery, B. H. Zhou, J. Lee, E.-S. Lee, E. M. Miller, R. Ihly, D. Wesenberg, K. S. Mistry, S. L. Guillot, B. L. Zink, Y.-H. Kim, J. L. Blackburn and A. J. Ferguson: Nature Energy **1** (2016) 16033.
- 12) K. Yanagi, S. Kanda, Y. Oshima, Y. Kitamura, H. Kawai, T. Yamamoto, T. Takenobu, Y. Nakai and Y. Maniwa: Nano Lett. **14**, (2014) 6437.
- 13) S. Shimizu, T. Iizuka, K. Kanahashi, J. Pu, K. Yanagi, T. Takenobu and Y. Iwasa: Small **12** (2016) 3388.
- 14) N. T. Hung, A. R. T. Nugraha, E. H. Hasdeo, M. S. Dresselhaus, and R. Saito: Phys. Rev. B **92**, 165426 (2015).
- 15) Y. Nonoguchi, K. Ohashi, R. Kanazawa, K. Ashiba, K. Hata, T. Nakagawa, C. Adachi, T. Tanase and T. Kawai: Scientific Reports, **3** (2013) 3344.
- 16) Y. Nonoguchi, M. Nakano, T. Murayama, H. Hagino, S. Hama, K. Miyazaki, R. Matsubara, M. Nakamura and T. Kawai: Adv. Funct. Mater., **26** (2016) 3021.
- 17) Y. Nonoguchi, A. Tani, T. Ikeda, C. Goto, N. Tanifuji, R. M. Uda, T. Kawai: Small **13** (2017) 1603420.
- 18) T. Fukumaru, T. Fujigaya and N. Nakashima: Sci. Rep. **5** (2015) 7951.
- 19) Y. Nakashima, N. Nakashima and T. Fujigaya: Synthetic Metals, **225** (2017) 76.
- 20) S. Horike, T. Fukushima, a T. Saito, T. Kuchimura, Y. Koshiba, M. Morimoto and K. Ishida: Mol. Syst. Des. Eng., **2** (2017) 616.
- 21) B. A. MacLeod, N. J. Stanton, I. E. Gould, D. Wesenberg, R. Ihly, Z. R. Owczarzyk, K. Hurst, C. S. Fewox, C. N. Folmar, K. Holman Hughes, B. L. Zink, J. Blackburn and A. J. Ferguson: Energy Environ. Sci., **10** (2017) 2168.
- 22) P. H. Jiang, H. J. Liu, D. D. Fan, L. Cheng, J. Wei, J. Zhang, J. H. Lianga and J. Shia: Phys. Chem. Chem. Phys., **17** (2015) 27558.
- 23) M. Ohnishi, T. Shiga and J. Shiomi: Phys. Rev. B **95** (2017) 155405.
- 24) T. Yamamoto and H. Fukuyama: J. Phys. Soc. Jpn. **82** (2018) 024707.

- 25) H. Fukuyama, Y. Fuseya, M. Ogata, A. Kobayashi and Y. Suzumura: *Physica B: Condensed Matter* **407** (2012) 1943.
- 26) J.S. Langer: *Phys. Rev.* **128** (1962) 1110.
- 27) V. Ambegaokar and A. Griffin: *Phys. Rev.* **137** (1965) 1151.
- 28) R. Kubo: *J. Phys. Soc. Jpn.* **12** (1957) 570.
- 29) J. M. Luttinger: *Phys. Rev.* **135** (1964) A1505.
- 30) M. Ogata and H. Fukuyama: submitted to JPSJ.
- 31) M. Jonson and G. D. Mahan: *Phys. Rev. B* **21** (1980) 4223.
- 32) A. Sommerfeld and H. Bethe: *Elektronentheorie der Metalle*, Handbuch der Physik **24/2** (1933) (Springer Verlag).
- 33) N. F. Mott and H. Jones: *The Theory of the Properties of Metals and Alloys* (1936) (Oxford).
- 34) A.H. Wilson: *The Theory of Metals* (1936) (Cambridge).
- 35) *Anderson Localization*, ed. Y. Nagaoka: *Prog. Theor. Phys. Supplement* **84** (1985).
- 36) N. F. Mott: *Phil. Mag.* **19** (1969) 835.
- 37) N. Hamada, S.-I. Sawada and A. Oshiyama: *Phys. Rev. Lett.* **68** (1992) 579.
- 38) R. Saito, M. Fujita, G. Dresselhaus and M. S Dresselhaus: *Appl. Phys. Lett.* **60** (1992) 2204.
- 39) N. F. Mott and E. A. Davis: *Electron Processes in Non-crystalline Materials* (Clarendon, Oxford, U.K., 1971) p. 47.
- 40) N. F. Mott and H. Jones: *The Theory of the Properties of Metals and Alloys* (Clarendon Press, Oxford, 1936).
- 41) A.F. Ioffe: *Semiconductor Thermoelements and Thermoelectric cooling*, (Infosearch Limited, London, 1957).
- 42) T. Saso: *Trans. MRS-J* **29** (2004) 2845.